

# Geophysical Research Letters<sup>®</sup>



## RESEARCH LETTER

10.1029/2023GL106617

Haoran Chu and Chang Cao contributed equally to this work.

### Key Points:

- A box model of moist static energy budget in the atmospheric boundary layer is developed for the land wet-bulb temperature change
- Wet-bulb temperature over global land changes 17% faster than ocean surface temperature
- A robust relationship exists between the wet-bulb temperature and the downward longwave radiation

### Supporting Information:

Supporting Information may be found in the online version of this article.

### Correspondence to:

X. Lee and W. Xiao,  
xuhui.lee@yale.edu;  
wei.xiao@nuist.edu.cn

### Citation:

Chu, H., Cao, C., Wang, W., Xiao, W., Zhang, K., Zhang, M., & Lee, X. (2024). The land wet-bulb temperature increases faster than the sea surface temperature. *Geophysical Research Letters*, 51, e2023GL106617. <https://doi.org/10.1029/2023GL106617>

Received 4 OCT 2023

Accepted 11 JAN 2024

### Author Contributions:

**Conceptualization:** Xuhui Lee  
**Formal analysis:** Haoran Chu, Chang Cao  
**Funding acquisition:** Chang Cao  
**Visualization:** Haoran Chu, Chang Cao, Wei Wang, Wei Xiao, Keer Zhang, Mi Zhang  
**Writing – original draft:** Haoran Chu, Chang Cao

© 2024. The Authors.

This is an open access article under the terms of the [Creative Commons Attribution-NonCommercial-NoDerivs](https://creativecommons.org/licenses/by/4.0/) License, which permits use and distribution in any medium, provided the original work is properly cited, the use is non-commercial and no modifications or adaptations are made.

## The Land Wet-Bulb Temperature Increases Faster Than the Sea Surface Temperature

Haoran Chu<sup>1,2</sup> , Chang Cao<sup>1,2</sup> , Wei Wang<sup>1,2</sup> , Wei Xiao<sup>1,2</sup> , Keer Zhang<sup>3</sup>, Mi Zhang<sup>1,2</sup>, and Xuhui Lee<sup>3</sup> 

<sup>1</sup>Center on Atmospheric Environment, International Joint Laboratory on Climate and Environment Change (ILCEC), Nanjing University of Information Science and Technology, Nanjing, China, <sup>2</sup>Key Laboratory of Meteorological Disaster, Ministry of Education and Collaborative Innovation Center on Forecast and Evaluation of Meteorological Disasters, Nanjing University of Information Science and Technology, Nanjing, China, <sup>3</sup>School of the Environment, Yale University, New Haven, CT, USA

**Abstract** Vapor buildup in the atmosphere and faster warming over land than over ocean are ubiquitous features of climate change. This combination is a threat to society because the associated heat stress may exceed the limit for human survival. The heat stress due to high humidity and high temperature is quantified with the wet-bulb temperature ( $T_w$ ). A common view is that the land  $T_w$  should change at the same rate as the ocean surface temperature ( $T_s$ ). Using climate model data and atmospheric observations, we show that the land  $T_w$  increases 17% faster than  $T_s$ . This amplification arises from stronger downward longwave radiation ( $L_d$ ) at the surface in a warmer climate, which causes moist static energy to accumulate in the atmospheric boundary layer. We also find that  $L_d$  is a better predictor of  $T_w$  than  $T_s$  at interannual to decadal time scales. These relationships are robust across climates and across model simulations.

**Plain Language Summary** Humid heat, or combination of high temperature and high humidity, is a serious climate threat to society. A robust understanding of the climatology of humid heat—as measured by the wet-bulb temperature  $T_w$ —is needed to inform strategies for heat risk mitigation. Here we perform a comprehensive analysis of  $T_w$  using atmospheric observations and climate model calculations, and develop a simple box model for the land humid heat. The relationship between this temperature and the longwave radiation energy can help future prediction of the land humid heat.

## 1. Introduction

Humid heat decreases labor efficiency and exacerbates heat stress risk (Davis et al., 2016; Dunne et al., 2013; Mora et al., 2017). The wet-bulb temperature ( $T_w$ ) is a humid heat index frequently used to approximate the skin temperature of a perspiring human body. High  $T_w$  conditions suppress the body's ability to dissipate its metabolic heat to the environment via perspiration. If  $T_w$  exceeds the threshold of 35°C, this cooling mechanism can no longer function, and the consequence is deadly (Sherwood & Huber, 2010). The past few decades have seen rapid increases in  $T_w$  (Raymond et al., 2020; Rogers et al., 2021; Speizer et al., 2022). Exceedance of the lethal limit of 35°C is projected to occur on land in the summer season near the end of the 21st century under high emission scenarios (Im et al., 2017; Kang & Eltahir, 2018; Pal & Eltahir, 2016). A robust understanding of how the land  $T_w$  changes with the energy and the water cycles is needed to inform strategies for mitigating the rising heat risk to society.

The wet-bulb temperature is a thermodynamic variable equivalent to the surface moist static energy (MSE; Eltahir & Pal, 1996; Raymond et al., 2021; Zhang et al., 2021). The land  $T_w$  is thought to be controlled by the ocean surface temperature ( $T_s$ ). At tropical latitudes (20°S to 20°N, except in some monsoon regions), the maximum surface MSE is uniform between land and ocean due to weak horizontal temperature gradients in the troposphere (Byrne & O'Gorman, 2018; Sobel & Bretherton, 2000; Zhang et al., 2021). An inference from the MSE conservation, supported by climate model calculations (Sherwood & Huber, 2010; Zhang et al., 2021), is that the land annual maximum  $T_w$  at these latitudes should change at about the same rate as the mean  $T_s$ . (The change of the land mean  $T_w$  at these latitudes is probably slower than the change of the mean  $T_s$ .) Other researchers have relaxed this equality relationship beyond the tropics and beyond the maximum state, hypothesizing that the mean MSE changes are equal over the global land and ocean (60°S to 80°N; Byrne & O'Gorman, 2018). According to this

hypothesis, the land mean  $T_w$  should increase at the same rate as  $T_s$ . This MSE conservation theory emphasizes oceanic control of the land  $T_w$ .

A competing hypothesis is that the land  $T_w$  should rise faster than  $T_s$ , on the account of the fact that land processes also exert strong influence on the surface MSE. In response to rising atmospheric  $\text{CO}_2$ , the land Bowen ratio will increase (Duan et al., 2020; Sherwood & Fu, 2014), shifting the surface enthalpy flux more toward sensible heat. The result is that the land temperature increases  $\sim 50\%$  faster than  $T_s$  (Joshi et al., 2008; Lambert & Chiang, 2007; Sutton et al., 2007). Because sensible heat is the dominant component of MSE (Matthews et al., 2022), this land-ocean warming contrast raises the possibility that the land  $T_w$  should also increase much faster than  $T_s$ . The role of latent heat is less clear. The widespread increase in land aridity and decrease in soil moisture (Berg et al., 2016; Dai, 2013; Huang et al., 2016; Mankin et al., 2019; Sherwood & Fu, 2014) suggest that the latent heat component of MSE should decrease over time, a deduction supported by some observational studies (Lutsko, 2021; Yu et al., 2021). Other studies have reported that, instead of offsetting each other, the latent MSE component change actually reinforces the sensible component increase (Matthews et al., 2022; Peterson et al., 2011; Stoy et al., 2022), further amplifying the  $T_w$  trend. A key obstacle to understanding the role of latent heat in  $T_w$  change is that humidity trend calculation is extremely sensitive to the choice of humidity variable.

In this study, we analyze the relationship between the land mean  $T_w$  and  $T_s$  using climate model outputs from the Coupled Model Intercomparison Project Phase 6 (CMIP6) and atmospheric observational data. The results are used to test the above two hypotheses, that  $T_w$  should change at the same rate as  $T_s$  or that it should change faster than  $T_s$ . Our specific goals are: (a) to develop a simple box model of the MSE budget of the atmospheric boundary layer (ABL) over land, (b) to compare changes in the land  $T_w$ , the atmospheric temperature on land ( $T_a$ ) and the sea surface temperature  $T_s$  in historical and future climates, and (c) to examine the relationship between the land  $T_w$  change and the change in the downward longwave radiation at the Earth's surface ( $L_\downarrow$ ). A consequence of climate warming is increase in  $L_\downarrow$  (Stephens & Hu, 2010). We are interested in whether  $L_\downarrow$  can serve as a predictor of future  $T_w$ .

Our results are restricted to the summer months (June-July-August in the Northern Hemisphere and December-January-February in the Southern Hemisphere). These months represent the hottest period of the year, coincide with high-humidity conditions in the wet season, and have the highest  $T_w$  of the year (Zhang et al., 2023).

## 2. Data Sets

### 2.1. Climate Model Data

We analyzed climate variables simulated by 37 CMIP6 climate models under five transient climate experiments, including Historical, SSP126, SSP245, SSP370, and SSP585 (Table S1 in Supporting Information S1). A total of 145 model simulations were used. The near-surface wet-bulb temperature  $T_w$  was calculated on a daily basis using daily mean air temperature, humidity and pressure. All model results are re-gridded onto common  $1^\circ \times 1^\circ$  grids using linear interpolation.

We focus on summer  $T_w$  climatology in land grid cells between  $60^\circ\text{S}$  and  $60^\circ\text{N}$ . Summer season is June to August in the Northern Hemisphere and December to February in the Southern Hemisphere. In our analysis,  $\Delta$  denotes time change in a variable, defined as the difference between the mean of the last 10 years (2004–2013 in Historical and 2090 to 2099 in other experiments) and the mean of the first 10 years (1850–1859 in Historical and 2015 to 2024 in other experiments). The 10-year averaging length is the same as in a study on the global hydrological sensitivity (Fläschner et al., 2016). The last years of Historical (2014) and future experiments (2100) are omitted due to unavailability of January and February data in 2015 and in 2101. (We need these months to compute summer statistics for the Southern Hemisphere.) Also note that  $\Delta$  is computed over a longer period for Historical (154 years) than for the other experiments (75 years). The sensitivity of  $T_w$  to the surface downward longwave radiation  $L_\downarrow$  was calculated with two methods. The first method was used to calculate the overall  $T_w$  versus  $L_\downarrow$  sensitivity from all the 145 model simulations. This was obtained through linear regression of  $\Delta T_w$  against  $\Delta L_\downarrow$ , with each sample representing one model simulation (Figure 3b below). The second method estimated the sensitivity for individual model simulations. In this method, the sensitivity was the linear regression slope of the summer mean  $T_w$  against the summer mean  $L_\downarrow$ , with each sample representing a summer value. An example of the second method is given in Figure 4b (inset) below. The second method provides more robust estimate of the sensitivity for an individual simulation than the ratio  $\Delta T_w / \Delta L_\downarrow$  because the former avoids errors associated with

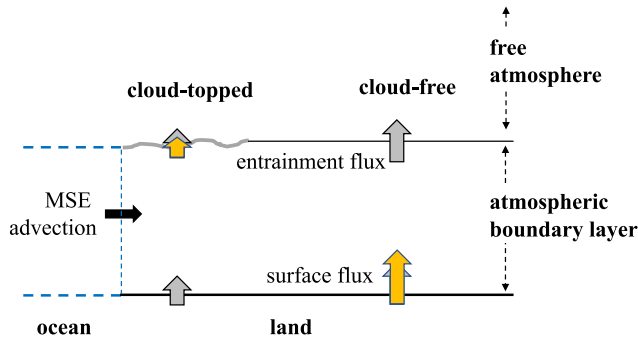


**Figure 1.** An advection-diffusion model of MSE in the land ABL. The accumulation of MSE in the land ABL is balanced by the MSE advected from the ocean, the surface enthalpy flux to the ABL and the entrainment enthalpy flux from the ABL to the free atmosphere. Orange arrows indicate flux responses to increase in downward longwave radiation.

division by extremely small numbers (especially for some SSP126 simulations). The second method was used to obtain scenario mean sensitivity and its spread (Figure 3a below).

## 2.2. Reanalysis and Observational Data

We compared the relationship between  $T_w$  and  $L_{\downarrow}$  from climate model simulations with the relationship found in two other data sets. The first data set consists of five atmospheric reanalysis data products. They are: ERA5 (Hersbach et al., 2020), JRA-55 (Kobayashi et al., 2015), MERRA-2 (Gelaro et al., 2017), NCEP-R1 (Kalnay et al., 1996) and NCEP-R2 (Kanamitsu et al., 2002). These products span a common 40-year period from 1980 to 2019, and the results are also interpolated onto  $1^{\circ} \times 1^{\circ}$  grids. Although reanalysis data are not strictly observations, they are generated from various sources of observational data through numerical models and data assimilation systems to best represent the state of historical climate.

The second data set consists of observations at 168 surface radiation measurement sites located on land between  $60^{\circ}\text{S}$  and  $60^{\circ}\text{N}$ . Of these, 136 are from the FLUXNET Network (Pastorello et al., 2020), seven from the U.S. Surface Radiation Budget Network (Augustine et al., 2000), 24 from the Baseline Surface Radiation Network (Driemel et al., 2018) and one from the Lake Taihu Eddy Flux Network (Zhang et al., 2020a; Figure S1a in Supporting Information S1). These sites have simultaneous observations of air temperature, humidity, atmospheric pressure and surface longwave radiation for at least four summers between 1991 and 2022.

In line with CMIP6 models,  $T_w$  was calculated at daily timesteps. The  $T_w$  versus  $L_{\downarrow}$  relationship was built on linear regression of summer means for reanalysis data. The observational relationship between  $T_w$  and  $L_{\downarrow}$  was based on linear regression of daily means from station data to avoid bad representation caused by data gaps at specific sites (Text S1 in Supporting Information S1).

## 2.3. Calculation of the Wet-Bulb Temperature

The wet-bulb temperature  $T_w$  is an implicit function of humidity ( $e_a$ ), air temperature ( $T_a$ ) and air pressure ( $P$ ). Some researchers have used regression models to approximate  $T_w$  from observations of  $e_a$ ,  $T_a$ , and  $P$  (Brimicombe et al., 2023; Kong & Huber, 2022). Here we used a numerical method, similar to those presented by Krakauer et al. (2020) and Davies-Jones (2008), to solve  $T_w$  from the wet-bulb equation (Equation 4 below) at the daily timestep. The numerical solution captures the nonlinear dependence of  $T_w$  on  $e_a$ ,  $T_a$ , and  $P$  (Davies-Jones, 2008).

## 3. An Advection-Diffusion Model of MSE on Land

Here, we present an advection-diffusion model of MSE in the land ABL (Figure 1). We begin the model derivation by presenting the definitions of MSE  $h$  ( $\text{J kg}^{-1}$ ) and equivalent temperature  $T_q$  (K) (Fischer & Knutti, 2013; Wallace & Hobbs, 2006)

$$h = c_p T_a + \lambda q_a + g z \quad (1)$$

$$T_q = T_a + e_a / \gamma \quad (2)$$

where  $c_p$  is the specific heat of air at constant pressure ( $\text{J kg}^{-1} \text{K}^{-1}$ ),  $\lambda$  is the latent heat of vapourization ( $\text{J kg}^{-1}$ ),  $T_a$  is air temperature (K),  $q_a$  is specific humidity ( $\text{kg kg}^{-1}$ ),  $e_a$  is vapor pressure (hPa),  $g$  is gravitational acceleration ( $\text{m s}^{-2}$ ),  $z$  is height ( $m$ ), and  $\gamma$  is the psychrometric constant ( $\text{hPa K}^{-1}$ ). These two quantities are related to each other, as

$$h = c_p T_q + g z \quad (3)$$

The wet-bulb temperature  $T_w$  (K) is governed by the wet-bulb equation (Lee, 2018)

$$T_w + e_w / \gamma = T_a + e_a / \gamma (= T_q) \quad (4)$$

where  $e_w$  (hPa) is the saturation vapor pressure at  $T_w$ . Equation 4 expresses  $T_w$  as an implicit function of air temperature  $T_a$  and vapor pressure  $e_a$ .

Let  $h_o$  be the MSE in the ocean ABL and  $h$  be the MSE in the land ABL at distance  $l$  ( $m$ ) from the land-ocean boundary. As air moves from the ocean to the land ABL, its MSE will increase due to the enthalpy flux from the land surface ( $F_s$ ,  $W m^{-2}$ ; Figure 1) and will decrease due to the entrainment enthalpy flux into the free atmosphere above ( $F_e$ ,  $W m^{-2}$ ; Figure 1). In steady state, conservation of MSE leads to

$$h = h_o + \frac{F_s - F_e}{\rho} \cdot \frac{l}{uz_i} \quad (5)$$

where  $u$  is wind speed ( $m s^{-1}$ ),  $\rho$  is air density ( $kg m^{-3}$ ), and  $z_i$  is ABL depth ( $m$ ). Equation 5 is an application of the ABL box model, and the product  $uz_i$  is known as the ventilation factor (Oke et al., 2017).

Differentiating Equation 5 over time, omitting changes in  $u$ ,  $z_i$ , and vertical movement ( $gz$ ), and using Equation 3, we obtain

$$\Delta T_q = \Delta T_{q,o} + \frac{\Delta(F_s - F_e)}{\rho c_p} \cdot \frac{l}{uz_i} \quad (6)$$

where  $T_{q,o}$  (K) is the equivalent temperature over the ocean surface. Differentiating Equation 4 and using a linear approximation to  $e_w$  as a function of  $T_w$ , we obtain

$$\Delta T_w = w(\Delta T_a + \Delta e_a/\gamma) \quad (7)$$

In this derivation, we have used the following relationship

$$\Delta T_w = w \Delta T_q \quad (8)$$

The scaling factor  $w$  in Equations 7 and 8 is given by

$$w = 1 / \left( 1 + \frac{\Delta w}{\gamma} \right) \quad (9)$$

where  $\Delta w$  ( $hPa K^{-1}$ ) is the slope of the saturation vapor pressure at  $T_w$ . A typical value of  $w$  is 0.3 (Zhang et al., 2023).

Combining Equations 6 and 8, and using the fact that change in the oceanic wet-bulb temperature is nearly identical to change in the ocean surface temperature  $T_s$  (K) (Figure S2 in Supporting Information S1), we obtain

$$\Delta T_w = \Delta T_s + w \frac{\Delta(F_s - F_e)}{\rho c_p} \cdot \frac{l}{uz_i} \quad (10)$$

We assume that change in the net enthalpy flux of the land ABL can be approximated by change in the net surface longwave radiation ( $W m^{-2}$ )

$$\Delta(F_s - F_e) \approx \Delta(L_1 - L_\uparrow) \quad (11)$$

where  $L_1$  is longwave radiation emitted by the surface. A ubiquitous feature of climate warming is that  $L_1$  will increase, and the rate of  $L_1$  increase is faster than that of  $L_\uparrow$  (Stephens et al., 2012; Wang et al., 2021). In the cloud-free portion of the ABL, this net gain of longwave radiation by the surface causes the surface enthalpy flux to rise (Figure 1, orange arrow). In the cloud-topped portion of the ABL, the cloud-top radiative cooling is reduced due to rising  $L_1$ , with a consequence being reduced entrainment rate (Stevens, 2006; Figure 1, orange arrow). Both processes lead to accumulation of MSE in the ABL relative to the MSE above the ocean surface. According to climate model calculations, change in the net surface longwave radiation is about 30% of change in the downward longwave radiation (Wang et al., 2021)

$$\Delta(L_1 - L_\uparrow) \approx 0.3 \Delta L_1 \quad (12)$$

Substituting Equations 11 and 12 into Equation 10, we obtain

$$\Delta T_w = \Delta T_s + \alpha \Delta L_1 \quad (13)$$

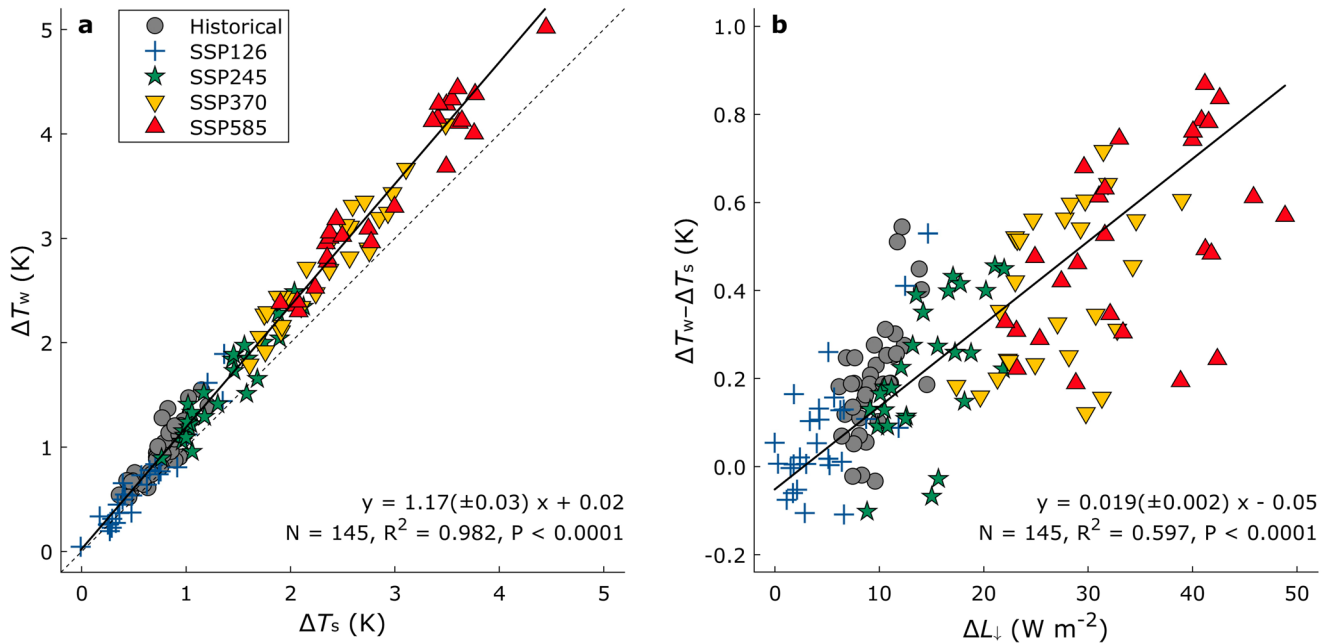


**Figure 2.** Amplification of the land wet-bulb temperature by the surface longwave radiative effect. (a) Relationship between change in the land wet-bulb temperature  $\Delta T_w$  and change in the ocean surface temperature  $\Delta T_s$ . (b) Difference between  $\Delta T_w$  and  $\Delta T_s$  as a function of the change in the surface downward longwave radiation  $\Delta L_{\downarrow}$ . Solid lines represent linear relationships with regression statistics noted. Dashed line in (a) is 1:1.

where the energy sensitivity factor  $\alpha$  (K per  $W m^{-2}$ ) is given by

$$\alpha \approx 0.3 \times \frac{w}{\rho c_p} \cdot \frac{l}{uz_i} \quad (14)$$

A scale analysis of Equation 14 shows that  $\alpha$  is on the order of  $1 \times 10^{-2}$  K per  $W m^{-2}$ . For example, based on typical values of 2,000 km,  $5 m s^{-1}$  and 1 km for  $l$ ,  $u$ , and  $z_i$ , respectively, Equation 14 gives  $\alpha$  of 0.03 K per  $W m^{-2}$ . Because  $\Delta L_{\downarrow}$  is positive in a warming climate, Equation 13 indicates that the land  $T_w$  change should be greater than the  $T_s$  change. Positive  $\Delta L_{\downarrow}$  is known to intensify the land hydrological cycle (Andrews et al., 2009; Wang et al., 2018).

## 4. Results

### 4.1. Amplification of the Land Wet-Bulb Temperature

The CMIP6 model results confirm a prediction of the ABL budget analysis (Equation 13), that the land  $T_w$  should change faster than  $T_s$ , as shown in Figure 2a. The rate of amplification is 17% across 145 model simulations under five transient climate experiments. For comparison, the rate of amplification of the summer surface air temperature  $T_a$  on land is 61% (Figure S3 in Supporting Information S1).

The model data also support the linear relationship between the  $T_w$  and  $T_s$  changes with the change in  $L_{\downarrow}$  (Figure 2b), yielding an energy sensitivity factor  $\alpha$  of 0.019 K per  $W m^{-2}$  on the same order of magnitude as that obtained from the scale analysis. The scale analysis omits changes to the surface enthalpy flux brought by changes in the downward solar radiation. As water vapor molecules accumulate in the atmospheric column, vapor absorption of solar radiation in near-infrared wavelengths (Pendergrass & Hartmann, 2014) offsets some of the net longwave radiation gained by the surface. As a result, the actual  $\alpha$  is smaller than if the longwave radiation were to act on the boundary-layer MSE alone. In the historical climate, dimming of solar radiation due to air pollution (Wild, 2016) also reduces the  $T_w$  sensitivity to the longwave radiative effect.

In the derivation of the box model, we have omitted changes in wind speed  $\Delta u$  and in the ABL depth  $\Delta z_i$ . Although the ABL depth is not a standard output variable of CMIP6 models, it is inversely proportional to the static stability of the free troposphere  $\Gamma$  (Barbaro et al., 2013; Tennekes, 1973), which in this study is calculated as

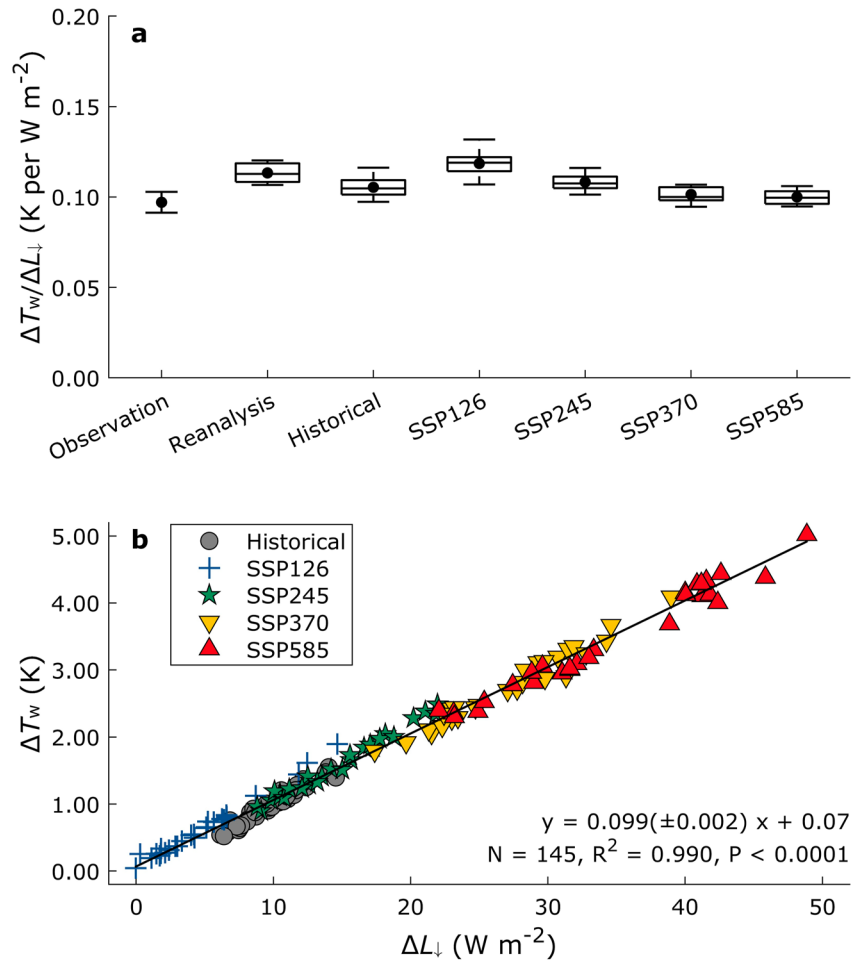


**Figure 3.** Tight relationship between the land wet-bulb temperature and the surface longwave radiation. (a) Sensitivity of the wet-bulb temperature  $T_w$  to the downward longwave radiation  $L_↓$  from observations, reanalyses and CMIP6 models. (b) Relationship between the  $T_w$  change and the  $L_↓$  change. Observational result in (a) is shown as mean (dot) and 95% confidence bound (error bars). Box plots show the median (line), 25%–75% range (box), 5%–95% range (whiskers) and the mean value (dot). Solid line in (b) represents linear relationship with regression statistics noted.

$$\Gamma = T_{700\text{mb}} - T_{2\text{m}} \quad (15)$$

where  $T_{700\text{mb}}$  and  $T_{2\text{m}}$  are temperature at the pressure height of 700 mb and at the screen height (2 m), respectively. The omission of  $\Delta u$  is defensible for scenario means (Figure S4a in Supporting Information S1), but individual model simulations can experience  $\Delta u$  up to 0.1–0.2 m s<sup>-1</sup> or about 4% relative change. The scenario mean  $\Delta\Gamma$  is negative for future climates (Figure S4b in Supporting Information S1), meaning that as the atmospheric CO<sub>2</sub> rises, the lower troposphere over land becomes progressively less stratified, and the ABL should become deeper. According to the box model (Equation 10), we expect  $\Delta T_w - \Delta T_s$  to be negatively correlated with  $\Delta u$  (and  $\Delta z_i$ ) and to be positively correlated with  $\Delta\Gamma$  through the influence of  $\Gamma$  on  $z_i$ . This expectation is based on the condition that as the climate warms up, change in the net enthalpy flux  $\Delta(F_s - F_e)$  is positive. This condition is generally satisfied according to Equation 11 because change in the net surface longwave radiation  $\Delta(L_↓ - L_↑)$  is positive (Wang et al., 2021). Putting it differently, if the ABL wind becomes stronger or if the stability of the lower troposphere becomes weaker in the future, the ABL will have a higher capacity to “ventilate,” with the result being more diluted MSE near the surface. A three-variable linear regression of all the 145 model simulations confirms this expectation, as the regression coefficient for  $\Delta u$  is negative and that for  $\Delta\Gamma$  is positive ( $R^2 = 0.67$ ,  $p < 0.0001$ ):

$$\Delta T_w - \Delta T_s = 0.0096 + 0.0165(\pm 0.0023)\Delta L_↓ - 0.7468(\pm 0.4014)\Delta u + 0.2499(\pm 0.1525)\Delta\Gamma \quad (16)$$

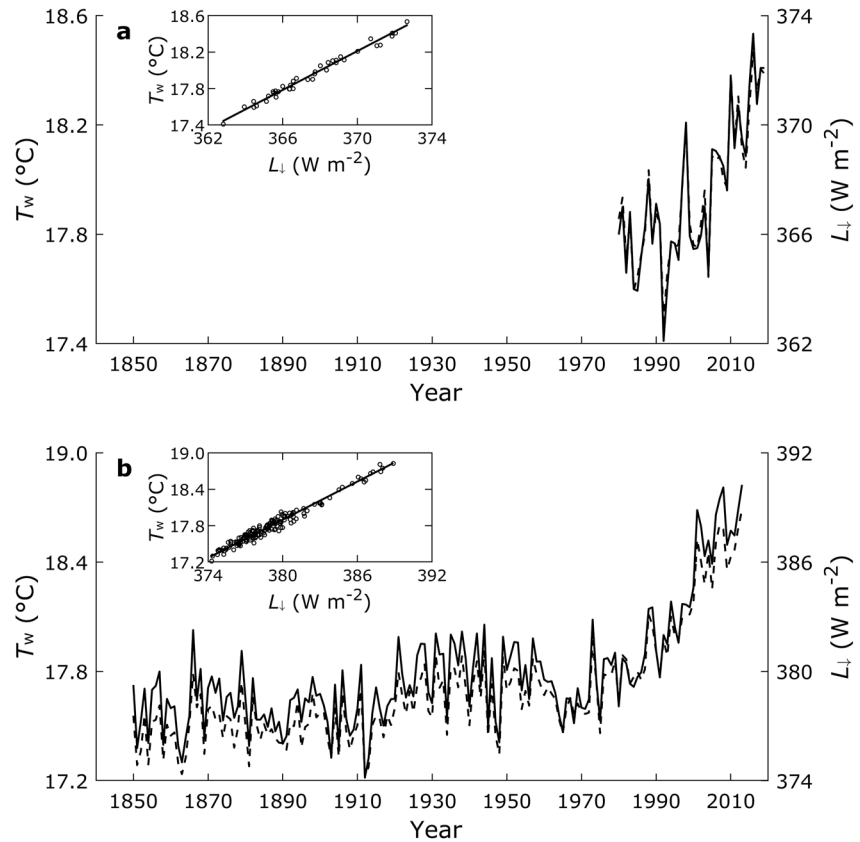


**Figure 4.** Significant correlation of the land wet-bulb temperature and the surface longwave radiation at interannual time scale. (a) Interannual changes of the wet-bulb temperature  $T_w$  and the surface downward longwave radiation  $L_d$  according to NCEP-R1 reanalysis. (b) As in (a) except from CESM2-WACCM historical model simulation. Solid and dashed lines represent  $T_w$  and  $L_d$ , respectively. Insets show scatter plots with linear regression  $T_w = 0.107 (\pm 0.005) L_d - 21.26$  ( $R^2 = 0.98$ ) for panel (a) and  $T_w = 0.105 (\pm 0.003) L_d - 21.91$  ( $R^2 = 0.97$ ) for panel (b).

#### 4.2. Relationship Between the Wet-Bulb Temperature and the Longwave Radiation

We now turn our attention to the direct dependence of the land  $T_w$  on the surface longwave radiation. The change in the land  $T_w$  is linearly correlated with the change in  $L_d$  (Figure 3b). This linear relationship is highly significant ( $p < 0.0001$ ) and explains 99% of the variations across the 145 model simulations. This correlation exists presumably because the MSE in the marine ABL is also modulated by the downward longwave radiation through its influence on the marine surface and entrainment enthalpy fluxes. The overall proportionality of  $\Delta T_w$  versus  $\Delta L_d$  is  $0.099 \pm 0.002$  K per  $\text{W m}^{-2}$  (mean  $\pm$  95% confidence bound). This apparent longwave sensitivity is about five times that of the sensitivity of the land  $T_w$  amplification to  $L_d$  (Figure 2b). The scenario mean sensitivity, that is, the mean sensitivity of model simulations under the same scenario, varies in a very narrow range from 0.100 K per  $\text{W m}^{-2}$  (SSP585; 5%–95% range: 0.095–0.106 K per  $\text{W m}^{-2}$ ) to 0.119 K per  $\text{W m}^{-2}$  (SSP126; 0.107–0.132 K per  $\text{W m}^{-2}$ ; Figure 3a).

The modeled  $T_w$  sensitivity to  $L_d$  is in excellent agreement with those obtained from two atmospheric data sets (Figure 3a). The first data set consists of five atmospheric reanalysis data products, covering the period from 1980 to 2019. The reanalysis mean sensitivity is  $0.113 \pm 0.006$  K per  $\text{W m}^{-2}$ .

The second data set consists of simultaneous observations of  $T_w$  and  $L_d$  at 168 surface radiation measurement sites on land. We calculated the sensitivity of  $T_w$  to  $L_d$  for each site using linear regression of daily summer observations. An example of such linear regression is given in Figure S1d in Supporting Information S1 for Bondville (BON), Illinois, United States, one of the longest running sites in our collection. Figure S1a in Supporting Information S1 shows the spatial distribution of the observed sensitivity of  $T_w$  to  $L_d$ . For comparison, Figure S1b in Supporting Information S1 is the global map of the mean sensitivity of the five reanalysis products. The two maps

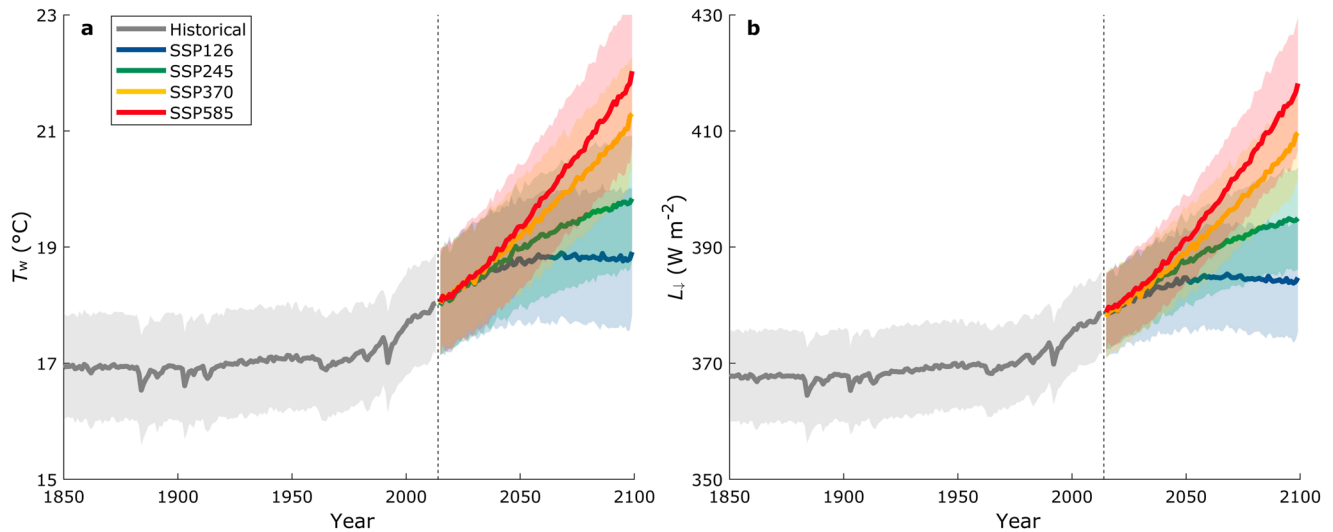


**Figure 5.** Long-term trends of the land wet-bulb temperature and the surface longwave radiation. (a) Multi-model mean time series of global (60°S–60°N) land summer wet-bulb temperature  $T_w$ . (b) As in (a) except for the surface downward longwave radiation  $L_d$ . Solid lines are multi-model means and shaded ranges are  $\pm 1$  standard deviation of the multi-model results. Vertical dashed line marks year 2014.

are highly correlated ( $p < 0.0001$ ). Because the observational sites are not evenly distributed across the world, a simple algebraic mean of the 168 sensitivity values is not representative of the true land mean sensitivity. To obtain an improved estimate of the global mean sensitivity of  $T_w$  to  $L_d$ , we first developed a linear relationship between the observed values and the reanalysis values from the grid cells where these sites are located (Figure S1c in Supporting Information S1). We then used this relationship to estimate the “observed” sensitivity for grid cells without observational data. Finally, we calculated the global mean sensitivity using these estimates. The mean sensitivity is  $0.097 \pm 0.006$  K per  $\text{W m}^{-2}$  (mean  $\pm$  95% confidence bound; Figure 3a), which is nearly identical to the overall modeled sensitivity (Figure 3b).

### 4.3. Temporal Variations of the Wet-Bulb Temperature and the Longwave Radiation

The summer mean  $T_w$  and  $L_d$  are highly correlated over time. Two examples of the interannual variations, one for an atmospheric reanalysis (NCEP-R1) and the other for a historical model simulation (CESM2-WACCM), are given in Figure 4. The coefficient of variation ( $R^2$ ) is 0.98 and 0.97 and the slope of the regression of  $T_w$  versus  $L_d$  is 0.107 and 0.105 K per  $\text{W m}^{-2}$ , for NCEP-R1 and CEMS2-WACCM, respectively. For the other four reanalysis products, ERA5, JRA-55, MERRA-2 and NCEP-R2, the  $R^2$  values are 0.95, 0.95, 0.99 and 0.98, and the regression slopes are 0.120, 0.113, 0.109, and 0.118 K per  $\text{W m}^{-2}$ , respectively. The  $R^2$  is greater than 0.90 for 143 (out of 145) model simulations.

On the climatic time scale, the multi-model mean  $T_w$  exhibits temporal trends that match nearly perfectly with the  $L_d$  trends (Figure 5). For example, the temporal correlation between the multi-model mean  $T_w$  and  $L_d$  is 1.00 for the SSP585 scenario. In the historical climate, volcanic eruptions cause the  $L_d$  to drop by 2.96, 2.53, and 3.09  $\text{W m}^{-2}$  in 1884, 1903, and 1992 from the value in the preceding years, and there is a proportional drop in  $T_w$  of 0.35, 0.31 and 0.36°C. In the SSP126 scenario, both  $L_d$  and  $T_w$  increase slowly from 2015 to 2060 and then level off beyond 2060.

The correlation pattern is consistent among inter-model, inter-scenario, and inter-annual variations (Figures 3–5). We suggest that the tight relationship between  $T_w$  and  $L_d$  is an intrinsic property of the climate system.

### 4.4. Results for the Tropical Zone

The above results are for the global land (60°S to 60°N). Recognizing that high humid heat regions are found mostly in the tropics, we have also analyzed the  $T_w$  climatology for the tropical zone (20°S to 20°N; Figure S5 in Supporting Information S1). In this band,  $T_s$  also changes at the same rate as the oceanic wet-bulb temperature.

The oceanic control on the land  $T_w$  change is still powerful ( $R^2 = 0.99$ ), but the amplification with respect to  $\Delta T_s$  is reduced to 7% from the global land value of 17%. Similarly, the amplification of the tropical land  $T_a$  is also reduced to a smaller amount (36%). The relationship between  $T_w$  and  $L_1$  is equally robust for the tropics ( $R^2 = 0.99$ ) as for the global land ( $R^2 = 0.99$ ; Figure 3b).

## 5. Summary and Discussion

In summary, we have shown that the land  $T_w$  change is amplified in reference to  $T_s$ , but at a smaller amount than the air temperature amplification. We argue that this amplification arises from the increase in  $L_1$ . Support for this argument is provided by a theoretical analysis of the MSE budget in the ABL on land. We also find a strong linear relationship between the  $T_w$  increase and the increase in  $L_1$ . The  $L_1$  increase is a predictable consequence of rising air temperature and rising air humidity in a warming climate (Stephens & Hu, 2010).

Time scale matters to the  $T_w$  climatology. Our results support the oceanic control hypothesis at long time scales of decades or longer (Byrne & O’Gorman, 2018). At these time scales, changes in  $T_s$  exert a dominant control on changes in the land  $T_w$ . In other words, future change of the humid heat stress on land is tightly coupled with ocean warming (Berg et al., 2016). The proportionality relation of  $\Delta T_w$  with  $\Delta T_s$  is equally powerful in explaining the inter-model and inter-scenario variations in  $T_w$  ( $R^2 = 0.98$ , Figure 2a) as the proportionality relation with  $\Delta L_1$  ( $R^2 = 0.99$ , Figure 3b). The land influence is smaller. Its role is to amplify the land  $T_w$  change by 17% beyond the baseline set by the  $T_s$  change. In relative terms, the land role in the total  $\Delta T_w$  is 14%. The relative contribution of the ocean influence is larger, at 86%. In absolute terms,  $T_s$  is projected to increase by 2.9 K at the end of the century, and the land influence amounts to an additional 0.5 K increase in  $T_w$ , according to multi-model simulations under the high emission scenario SSP585 (Figure 2a). In this regard, the box model can be considered as a refinement of the oceanic control hypothesis.

At the interannual time scale,  $L_1$  is a much better predictor of  $T_w$  variations than  $T_s$ . Years with higher  $L_1$  are associated with proportionally higher  $T_w$ , yielding a coefficient of variation  $R^2$  greater than 0.96 (Figure 4). In comparison, the correlation of interannual variations in  $T_s$  and  $T_w$  is weaker ( $R^2 < 0.64$ ; Figure S6 in Supporting Information S1). (Between 1950 and 1970,  $T_w$  and  $T_s$  are actually anti-correlated.) It appears that land processes are responsible for the interannual variabilities of the land  $T_w$ . In addition to enhancing the surface enthalpy flux and suppressing the entrainment enthalpy flux (Figure 1), higher  $L_1$  tends to occur under stronger static stability of the lower troposphere (Figure S7 in Supporting Information S1). It is well established that the growth of the land ABL is suppressed in a more stable troposphere (Barbaro et al., 2013; Tennekes, 1973). A shallower ABL favors accumulation of MSE near the surface (Mishra et al., 2020) and further reinforces the correlation between  $T_w$  and  $L_1$ .

It appears that the tight relationship between  $T_w$  and  $L_1$  is a fundamental property of the climate system. This relationship is found in model simulations (Figure 3b), in atmospheric reanalysis (Figure 4a) and in observational data (Figure S1d in Supporting Information S1). Since the  $L_1$  change is tied to changes in air temperature and air humidity (Stephens & Hu, 2010), the relationship may arise from the fact that both  $T_w$  and  $L_1$  co-vary with temperature and humidity. Although it is certainly a contributor, this mathematical coincidence is unlikely to be the mechanism that underlies the nearly perfect correlation between  $\Delta T_w$  and  $\Delta L_1$  at multiple time scales and across climate model simulations. This is because  $\Delta L_1$  measures the change of physical states of the atmospheric column, whereas  $\Delta T_w$  measures the change of MSE at the surface. The main source of  $L_1$  is radiation emission from water vapor molecules in the troposphere (Pendergrass & Hartmann, 2014; Stephens & Hu, 2010). Temporal and spatial variations of  $L_1$  are controlled by variations of the temperature of the whole atmospheric column and the total amount of water vapor in the column. Although the column mean temperature and humidity are correlated with the surface temperature and humidity, these correlations cannot accommodate tropospheric temperature and humidity adjustments to the CO<sub>2</sub> buildup (Soden & Held, 2006) and changes in atmospheric moisture transport (Trenberth, 2011). A more logical explanation is that the  $\Delta T_w$  dependence on  $\Delta L_1$  emerges from the physical regulations imposed by  $L_1$  on the MSE exchange between the ABL, the surface and the free troposphere (Figure 1).

Although our results pertain to summer and global mean states, they can inform the development of a predictive framework for  $T_w$  at finer time and spatial scales. Identifying conditions conducive to high  $L_1$ , such as strong tropospheric stability (Raymond et al., 2021), and shallowness of the ABL (Mishra et al., 2020) may improve the

prediction of extreme humid heat episodes. We wish to point out that humid heat behaves differently from dry heat in the ABL on land. (Humid heat is measured by  $T_w$  and dry heat is measured by  $T_a$ .) In particular, reduction in entrainment suppresses air temperature rise in the ABL (Lee, 2018) and therefore the dry heat intensity, but it enhances humid heat as discussed above.

The tight relationship between  $T_w$  and  $L_1$  presented in this study is a global mean property. Whether this relationship holds for extreme  $T_w$  and how the relationship in a specific location is linked to the local hydrological cycle are yet to be determined. Another limitation of this study is that daily mean variables may be inadequate for quantifying extreme heat. Future efforts should investigate patterns and processes at hourly timesteps.

### Conflict of Interest

The authors declare no conflicts of interest relevant to this study.

### Data Availability Statement

All data used in this study are publicly available. CMIP6 model data are available at <https://esgf-node.llnl.gov/search/cmip6/>. Models analyzed are listed in Table S1 in Supporting Information S1. Reanalysis data are available from the following sources: ERA5 at Hersbach et al. (2023a, 2023b), JRA-55 at Japan Meteorological Agency/Japan (2013a, 2013b), MERRA-2 at Global Modeling and Assimilation Office (GMAO) (2015a, 2015b), NCEP-R1 at <https://psl.noaa.gov/data/gridded/data.ncep.reanalysis.html>, and NCEP-R2 at <https://psl.noaa.gov/data/gridded/data.ncep.reanalysis2.html>. Observational data are available from the following sources: the FLUXNET2015 data set at <https://fluxnet.org/data/fluxnet2015-dataset/>, the U.S. Surface Radiation Budget Network data at <https://gml.noaa.gov/aftp/data/radiation/surfrad/>, the Baseline Surface Radiation Network data at <https://bsrn.awi.de/data/data-retrieval-via-pangaea/>, and the Lake Taihu Eddy Flux Network data at Zhang et al. (2020b). The computer codes used to produce the data graphs are available from the authors upon request.

### References

- Andrews, T., Forster, P. M., & Gregory, J. M. (2009). A surface energy perspective on climate change. *Journal of Climate*, 22(10), 2557–2570. <https://doi.org/10.1175/2008JCLI2759.1>
- Augustine, J. A., DeLuisi, J. J., & Long, C. N. (2000). SURFRAD—A national surface radiation budget network for atmospheric research. *Bulletin of the American Meteorological Society*, 81(10), 2341–2358. [https://doi.org/10.1175/1520-0477\(2000\)081<2341:SANSRB>2.3.CO;2](https://doi.org/10.1175/1520-0477(2000)081<2341:SANSRB>2.3.CO;2)
- Barbaro, E., Vilà-Guerau de Arellano, J., Krol, M. C., & Holtslag, A. A. M. (2013). Impacts of aerosol shortwave radiation absorption on the dynamics of an idealized convective atmospheric boundary layer. *Boundary-Layer Meteorology*, 148(1), 31–49. <https://doi.org/10.1007/s10546-013-9800-7>
- Berg, A., Findell, K., Lintner, B., Giannini, A., Seneviratne, S. I., van den Hurk, B., et al. (2016). Land-atmosphere feedbacks amplify aridity increase over land under global warming. *Nature Climate Change*, 6(9), 869–874. <https://doi.org/10.1038/nclimate3029>
- Brimicombe, C., Lo, C. H. B., Pappenberger, F., Di Napoli, C., Maciel, P., Quintino, T., et al. (2023). Wet bulb globe temperature: Indicating extreme heat risk on a global grid. *GeoHealth*, 7(2), e2022GH000701. <https://doi.org/10.1029/2022GH000701>
- Byrne, M. P., & O’Gorman, P. A. (2018). Trends in continental temperature and humidity directly linked to ocean warming. *Proceedings of the National Academy of Sciences of the United States of America*, 115(19), 4863–4868. <https://doi.org/10.1073/pnas.1722312115>
- Dai, A. (2013). Increasing drought under global warming in observations and models. *Nature Climate Change*, 3(1), 52–58. <https://doi.org/10.1038/nclimate1633>
- Davies-Jones, R. (2008). An efficient and accurate method for computing the wet-bulb temperature along Pseudoadiabats. *Monthly Weather Review*, 136(7), 2764–2785. <https://doi.org/10.1175/2007MWR2224.1>
- Davis, R. E., McGregor, G. R., & Enfield, K. B. (2016). Humidity: A review and primer on atmospheric moisture and human health. *Environmental Research*, 144, 106–116. <https://doi.org/10.1016/j.envres.2015.10.014>
- Driemel, A., Augustine, J., Behrens, K., Colle, S., Cox, C., Cuevas-Agulló, E., et al. (2018). Baseline surface radiation network (BSRN): Structure and data description (1992–2017). *Earth System Science Data*, 10(3), 1491–1501. <https://doi.org/10.5194/essd-10-1491-2018>
- Duan, S. Q., Findell, K. L., & Wright, J. S. (2020). Three regimes of temperature distribution change over dry land, moist land, and oceanic surfaces. *Geophysical Research Letters*, 47(24), e2020GL090997. <https://doi.org/10.1029/2020GL090997>
- Dunne, J. P., Stouffer, R. J., & John, J. G. (2013). Reductions in labour capacity from heat stress under climate warming. *Nature Climate Change*, 3(6), 563–566. <https://doi.org/10.1038/nclimate1827>
- Eltahir, E. A. B., & Pal, J. S. (1996). Relationship between surface conditions and subsequent rainfall in convective storms. *Journal of Geophysical Research*, 101(D21), 26237–26245. <https://doi.org/10.1029/96JD01380>
- Fischer, E. M., & Knutti, R. (2013). Robust projections of combined humidity and temperature extremes. *Nature Climate Change*, 3(2), 126–130. <https://doi.org/10.1038/nclimate1682>
- Fläschner, D., Mauritsen, T., & Stevens, B. (2016). Understanding the intermodel spread in global-mean hydrological sensitivity. *Journal of Climate*, 29(2), 801–817. <https://doi.org/10.1175/JCLI-D-15-0351.1>
- Gelaro, R., McCarty, W., Suárez, M. J., Todling, R., Molod, A., Takacs, L., et al. (2017). The modern-era retrospective analysis for research and applications, version 2 (MERRA-2). *Journal of Climate*, 30(14), 5419–5454. <https://doi.org/10.1175/JCLI-D-16-0758.1>
- Global Modeling, & Assimilation Office (GMAO). (2015a). MERRA-2 tavg\_1\_2d\_slv\_Nx: 2d, 1-hourly, time-averaged, single-level, assimilation, single-level diagnostics V5.12.4 [Dataset]. Goddard Earth Sciences Data and Information Services Center (GES DISC). <https://doi.org/10.5067/VJAFPL1ICSIV>

### Acknowledgments

C.C. acknowledges support by the National Natural Science Foundation of China (Grants 42021004 and 42005143) and the National Key R&D Program of China (Grant 2019YFA0607202). W.X. acknowledges support by the National Key R&D Program of China (Grant 2020YFA0607501), the Jiangsu Natural Science Foundation for Distinguished Young Scholar (BK20220055), the 333 Project of Jiangsu Province (BRA2017402) and the R&D Foundation of Jiangsu Province, China (BK20220020). K.Z. acknowledges support by a Yale Graduate Fellowship.

- Global Modeling, & Assimilation Office (GMAO). (2015b). MERRA-2 tavgM\_2d\_rad\_Nx: 2d, monthly mean, time-averaged, single-level, assimilation, radiation diagnostics V5.12.4 [Dataset]. Goddard Earth Sciences Data and Information Services Center (GES DISC). <https://doi.org/10.5067/OU3HJDS97300>
- Hersbach, H., Bell, B., Berrisford, P., Biavati, G., Horányi, A., Muñoz Sabater, J., et al. (2023a). ERA5 hourly data on single levels from 1940 to present [Dataset]. Copernicus Climate Change Service (C3S) Climate Data Store (CDS). <https://doi.org/10.24381/cds.adbb2d47>
- Hersbach, H., Bell, B., Berrisford, P., Biavati, G., Horányi, A., Muñoz Sabater, J., et al. (2023b). ERA5 monthly averaged data on single levels from 1940 to present [Dataset]. Copernicus Climate Change Service (C3S) Climate Data Store (CDS). <https://doi.org/10.24381/cds.f17050d7>
- Hersbach, H., Bell, B., Berrisford, P., Hirahara, S., Horányi, A., Muñoz-Sabater, J., et al. (2020). The ERA5 global reanalysis. *Quarterly Journal of the Royal Meteorological Society*, 146(730), 1999–2049. <https://doi.org/10.1002/qj.3803>
- Huang, J., Yu, H., Guan, X., Wang, G., & Guo, R. (2016). Accelerated dryland expansion under climate change. *Nature Climate Change*, 6(2), 166–171. <https://doi.org/10.1038/nclimate2837>
- Im, E. S., Pal, J. S., & Eltahir, E. A. B. (2017). Deadly heat waves projected in the densely populated agricultural regions of South Asia. *Science Advances*, 3(8), e1603322. <https://doi.org/10.1126/sciadv.1603322>
- Japan Meteorological Agency/Japan. (2013a). JRA-55: Japanese 55-year reanalysis, daily 3-hourly and 6-hourly data (updated monthly) [Dataset]. Research Data Archive at the National Center for Atmospheric Research, Computational and Information Systems Laboratory. <https://doi.org/10.5065/D6HH6H41>
- Japan Meteorological Agency/Japan. (2013b). JRA-55: Japanese 55-year reanalysis, monthly means and variances (updated irregularly) [Dataset]. Research Data Archive at the National Center for Atmospheric Research, Computational and Information Systems Laboratory. <https://doi.org/10.5065/D60G3H5B>
- Joshi, M. M., Gregory, J. M., Webb, M. J., Sexton, D. M. H., & Johns, T. C. (2008). Mechanisms for the land/sea warming contrast exhibited by simulations of climate change. *Climate Dynamics*, 30(5), 455–465. <https://doi.org/10.1007/s00382-007-0306-1>
- Kalnay, E., Kanamitsu, M., Kistler, R., Collins, W., Deaven, D., Gandin, L., et al. (1996). The NCEP/NCAR 40-year reanalysis project. *Bulletin of the American Meteorological Society*, 77(3), 437–472. [https://doi.org/10.1175/1520-0477\(1996\)077<0437:TNYRP>2.0.CO;2](https://doi.org/10.1175/1520-0477(1996)077<0437:TNYRP>2.0.CO;2)
- Kanamitsu, M., Ebisuzaki, W., Woollen, J., Yang, S.-K., Hnilo, J. J., Fiorino, M., & Potter, G. L. (2002). NCEP-DOE AMIP-II reanalysis (R-2). *Bulletin of the American Meteorological Society*, 83(11), 1631–1644. <https://doi.org/10.1175/BAMS-83-11-1631>
- Kang, S., & Eltahir, E. A. B. (2018). North China Plain threatened by deadly heatwaves due to climate change and irrigation. *Nature Communications*, 9(1), 2894. <https://doi.org/10.1038/s41467-018-05252-y>
- Kobayashi, S., Ota, Y., Harada, Y., Ebata, A., Moriya, M., Onoda, H., et al. (2015). The JRA-55 reanalysis: General specifications and basic characteristics. *Journal of the Meteorological Society of Japan*, 93(1), 5–48. <https://doi.org/10.2151/jmsj.2015-001>
- Kong, Q., & Huber, M. (2022). Explicit calculations of wet-bulb globe temperature compared with approximations and why it matters for labor productivity. *Earth's Future*, 10(3), e2021EF002334. <https://doi.org/10.1029/2021EF002334>
- Krakauer, N. Y., Cook, B. I., & Puma, M. J. (2020). Effect of irrigation on humid heat extremes. *Environmental Research Letters*, 15(9), 094010. <https://doi.org/10.1088/1748-9326/ab9ecf>
- Lambert, F. H., & Chiang, J. C. H. (2007). Control of land-ocean temperature contrast by ocean heat uptake. *Geophysical Research Letters*, 34(13), L13704. <https://doi.org/10.1029/2007GL029755>
- Lee, X. (2018). *Fundamentals of boundary-layer meteorology*. Springer International Publishing.
- Lutsko, N. J. (2021). The relative contributions of temperature and moisture to heat stress changes under warming. *Journal of Climate*, 34(3), 901–917. <https://doi.org/10.1175/JCLI-D-20-0262.1>
- Mankin, J. S., Seager, R., Smerdon, J. E., Cook, B. I., & Williams, A. P. (2019). Mid-latitude freshwater availability reduced by projected vegetation responses to climate change. *Nature Geoscience*, 12(12), 983–988. <https://doi.org/10.1038/s41561-019-0480-x>
- Matthews, T., Byrne, M., Horton, R., Murphy, C., Pielke Sr, R., Raymond, C., et al. (2022). Latent heat must be visible in climate communications. *WIREs Climate Change*, 13(4), e779. <https://doi.org/10.1002/wcc.779>
- Mishra, V., Ambika, A. K., Asoka, A., Aadhar, S., Buzan, J., Kumar, R., & Huber, M. (2020). Moist heat stress extremes in India enhanced by irrigation. *Nature Geoscience*, 13(11), 722–728. <https://doi.org/10.1038/s41561-020-00650-8>
- Mora, C., Dousset, B., Caldwell, I. R., Powell, F. E., Geronimo, R. C., Bielecki, C. R., et al. (2017). Global risk of deadly heat. *Nature Climate Change*, 7(7), 501–506. <https://doi.org/10.1038/nclimate3322>
- Oke, T. R., Mills, G., Christen, A., & Voogt, J. A. (2017). *Urban climates*. Cambridge University Press.
- Pal, J. S., & Eltahir, E. A. B. (2016). Future temperature in southwest Asia projected to exceed a threshold for human adaptability. *Nature Climate Change*, 6(2), 197–200. <https://doi.org/10.1038/nclimate2833>
- Pastorello, G., Trotta, C., Canfora, E., Chu, H., Christianson, D., Cheah, Y.-W., et al. (2020). The FLUXNET2015 dataset and the ONEFlux processing pipeline for eddy covariance data. *Scientific Data*, 7(1), 225. <https://doi.org/10.1038/s41597-020-0534-3>
- Pendergrass, A. G., & Hartmann, D. L. (2014). The atmospheric energy constraint on global-mean precipitation change. *Journal of Climate*, 27(2), 757–768. <https://doi.org/10.1175/JCLI-D-13-00163.1>
- Peterson, T. C., Willett, K. M., & Thorne, P. W. (2011). Observed changes in surface atmospheric energy over land. *Geophysical Research Letters*, 38(16), L16707. <https://doi.org/10.1029/2011GL048442>
- Raymond, C., Matthews, T., & Horton, R. M. (2020). The emergence of heat and humidity too severe for human tolerance. *Science Advances*, 6(19), eaaw1838. <https://doi.org/10.1126/sciadv.aaw1838>
- Raymond, C., Matthews, T., Horton, R. M., Fischer, E. M., Fueglistaler, S., Ivanovich, C., et al. (2021). On the controlling factors for globally extreme humid heat. *Geophysical Research Letters*, 48(23), e2021GL096082. <https://doi.org/10.1029/2021GL096082>
- Rogers, C. D. W., Ting, M., Li, C., Kornhuber, K., Coffel, E. D., Horton, R. M., et al. (2021). Recent increases in exposure to extreme humid-heat events disproportionately affect populated regions. *Geophysical Research Letters*, 48(19), e2021GL094183. <https://doi.org/10.1029/2021GL094183>
- Sherwood, S., & Fu, Q. (2014). A drier future? *Science*, 343(6172), 737–739. <https://doi.org/10.1126/science.1247620>
- Sherwood, S. C., & Huber, M. (2010). An adaptability limit to climate change due to heat stress. *Proceedings of the National Academy of Sciences of the United States of America*, 107(21), 9552–9555. <https://doi.org/10.1073/pnas.0913352107>
- Sobel, A. H., & Bretherton, C. S. (2000). Modeling tropical precipitation in a single column. *Journal of Climate*, 13(24), 4378–4392. [https://doi.org/10.1175/1520-0442\(2000\)013<4378:MTPIAS>2.0.CO;2](https://doi.org/10.1175/1520-0442(2000)013<4378:MTPIAS>2.0.CO;2)
- Soden, B. J., & Held, I. M. (2006). An assessment of climate feedbacks in coupled ocean-atmosphere models. *Journal of Climate*, 19(14), 3354–3360. <https://doi.org/10.1175/JCLI3799.1>
- Speizer, S., Raymond, C., Ivanovich, C., & Horton, R. M. (2022). Concentrated and intensifying humid heat extremes in the IPCC AR6 regions. *Geophysical Research Letters*, 49(5), e2021GL097261. <https://doi.org/10.1029/2021GL097261>

- Stephens, G. L., & Hu, Y. (2010). Are climate-related changes to the character of global-mean precipitation predictable? *Environmental Research Letters*, *5*(2), 025209. <https://doi.org/10.1088/1748-9326/5/2/025209>
- Stephens, G. L., Li, J., Wild, M., Clayson, C. A., Loeb, N., Kato, S., et al. (2012). An update on Earth's energy balance in light of the latest global observations. *Nature Geoscience*, *5*(10), 691–696. <https://doi.org/10.1038/ngeo1580>
- Stevens, B. (2006). Bulk boundary-layer concepts for simplified models of tropical dynamics. *Theoretical and Computational Fluid Dynamics*, *20*(5–6), 279–304. <https://doi.org/10.1007/s00162-006-0032-z>
- Stoy, P. C., Roh, J., & Bromley, G. T. (2022). It's the heat and the humidity: The complementary roles of temperature and specific humidity to recent changes in the energy content of the near-surface atmosphere. *Geophysical Research Letters*, *49*(4), e2021GL096628. <https://doi.org/10.1029/2021GL096628>
- Sutton, R. T., Dong, B., & Gregory, J. M. (2007). Land/sea warming ratio in response to climate change: IPCC AR4 model results and comparison with observations. *Geophysical Research Letters*, *34*(2), L02701. <https://doi.org/10.1029/2006GL028164>
- Tennekes, H. (1973). A model for the dynamics of the inversion above a convective boundary layer. *Journal of the Atmospheric Sciences*, *30*(4), 558–567. [https://doi.org/10.1175/1520-0469\(1973\)030<0558:AMFTDO>2.0.CO;2](https://doi.org/10.1175/1520-0469(1973)030<0558:AMFTDO>2.0.CO;2)
- Trenberth, K. E. (2011). Changes in precipitation with climate change. *Climate Research*, *47*(1–2), 123–138. <https://doi.org/10.3354/cr00953>
- Wallace, J. M., & Hobbs, P. V. (2006). *Atmospheric science: An introductory survey*. Elsevier Academic Press.
- Wang, W., Chakraborty, T. C., Xiao, W., & Lee, X. (2021). Ocean surface energy balance allows a constraint on the sensitivity of precipitation to global warming. *Nature Communications*, *12*(1), 2115. <https://doi.org/10.1038/s41467-021-22406-7>
- Wang, W., Lee, X., Xiao, W., Liu, S., Schultz, N., Wang, Y., et al. (2018). Global lake evaporation accelerated by changes in surface energy allocation in a warmer climate. *Nature Geoscience*, *11*(6), 410–414. <https://doi.org/10.1038/s41561-018-0114-8>
- Wild, M. (2016). Decadal changes in radiative fluxes at land and ocean surfaces and their relevance for global warming. *WIREs Climate Change*, *7*(1), 91–107. <https://doi.org/10.1002/wcc.372>
- Yu, S., Tett, S. F. B., Freychet, N., & Yan, Z. (2021). Changes in regional wet heatwave in Eurasia during summer (1979–2017). *Environmental Research Letters*, *16*(6), 064094. <https://doi.org/10.1088/1748-9326/ac0745>
- Zhang, K., Cao, C., Chu, H., Zhao, L., Zhao, J., & Lee, X. (2023). Increased heat risk in wet climate induced by urban humid heat. *Nature*, *617*(7962), 738–742. <https://doi.org/10.1038/s41586-023-05911-1>
- Zhang, Y., Held, I., & Fueglistaler, S. (2021). Projections of tropical heat stress constrained by atmospheric dynamics. *Nature Geoscience*, *14*(3), 133–137. <https://doi.org/10.1038/s41561-021-00695-3>
- Zhang, Z., Zhang, M., Cao, C., Wang, W., Xiao, W., Xie, C., et al. (2020a). A dataset of microclimate and radiation and energy fluxes from the Lake Taihu eddy flux network. *Earth System Science Data*, *12*(4), 2635–2645. <https://doi.org/10.5194/essd-12-2635-2020>
- Zhang, Z., Zhang, M., Cao, C., Wang, W., Xiao, W., Xie, C., et al. (2020b). A dataset of microclimate and radiation and energy fluxes from the Lake Taihu Eddy Flux Network [Dataset]. Harvard Dataverse, V2, *12*, 2635–2645. <https://doi.org/10.7910/DVN/HEWCWM>

*Geophysical Research Letters*

Supporting Information for

**The land wet-bulb temperature increases faster than the sea surface temperature**

Haoran Chu<sup>1,2†</sup>, Chang Cao<sup>1,2†</sup>, Wei Wang<sup>1,2</sup>, Wei Xiao<sup>1,2</sup>, Keer Zhang<sup>3</sup>, Mi Zhang<sup>1,2</sup>, and Xuhui Lee<sup>3</sup>

<sup>1</sup>Center on Atmospheric Environment, International Joint Laboratory on Climate and Environment Change (ILCEC), Nanjing University of Information Science and Technology, Nanjing, China, <sup>2</sup>Key Laboratory of Meteorological Disaster, Ministry of Education and Collaborative Innovation Center on Forecast and Evaluation of Meteorological Disasters, Nanjing University of Information Science and Technology, Nanjing, China, <sup>3</sup>School of the Environment, Yale University, New Haven, CT, USA

**Contents of this file**

Text S1  
Table S1  
Figures S1 to S7

**Introduction**

This supporting information contains additional texts, tables and figures referenced in the main text.

### **Text S1. Observed sensitivity of $T_w$ to $L_{\downarrow}$**

In our study, the modelled relationship between  $T_w$  and  $L_{\downarrow}$  was evaluated against observations at 168 radiation measurement sites on land between 60°S and 60°N. These sites were selected from the FLUXNET Network (Pastorello et al., 2020), the U.S. Surface Radiation Budget Network (Augustine et al., 2000), the Baseline Surface Radiation Network (Driemel et al., 2018) and the Lake Taihu Eddy Flux Network (Zhang et al., 2020).

We developed a set of standards for site selection. First, sites located outside the spatial scope of our study are excluded. In other words, we do not consider high-latitude sites or ocean sites that are located on small islands. Second, sites without concurrent temperature, humidity, and pressure measurements are excluded. Third, we evaluate data quality of each site by visually checking the raw time series of longwave radiation, humidity, air temperature and air pressure. Data records that fall out of the physically possible range, that show sudden step changes, and that do not follow the pattern of seasonal change of any variable are deleted. Fourth, sites with observational length less than four summers are excluded. We need enough data samples to ensure the statistical reliability of site-specific  $T_w$  versus  $L_{\downarrow}$  relationship. A total of 168 sites remains in our collection after we applied these data screening criteria.

We used daily values of air temperature, humidity and air pressure to calculate the daily  $T_w$ . Only data in the summer season were used. The sensitivity of  $T_w$  to  $L_{\downarrow}$  for each site was obtained as the linear regression slope of  $T_w$  versus  $L_{\downarrow}$ . An example is given in Figure S1d. We based our results on daily observations instead of summer means to avoid bad representation caused by data gaps at a specific site.

**Table S1.** CMIP6 models used in this study. Letter “Y” denotes data availability.

<b>Models</b>	<b>Native resolution</b>	<b>Historical</b>	<b>SSP126</b>	<b>SSP245</b>	<b>SSP370</b>	<b>SSP585</b>
ACCESS-CM2	144 × 192	Y	Y	Y	Y	Y
ACCESS-ESM1-5	145 × 192	Y	Y	Y	Y	Y
AWI-CM-1-1-MR	192 × 384	Y	Y	Y	Y	Y
AWI-ESM-1-1-LR	96 × 192	Y				
BCC-CSM2-MR	160 × 320	Y	Y	Y	Y	Y
CanESM5	64 × 128	Y	Y	Y	Y	Y
CESM2	192 × 288	Y				
CESM2-FV2	96 × 144	Y				
CESM2-WACCM	192 × 288	Y	Y	Y	Y	Y
CESM2-WACCM-FV2	96 × 144	Y				
CMCC-CM2-HR4	192 × 288	Y				
CMCC-CM2-SR5	192 × 288	Y	Y	Y	Y	Y
CMCC-ESM2	192 × 288	Y	Y	Y	Y	Y
EC-Earth3	256 × 512	Y	Y	Y	Y	Y
EC-Earth3-AerChem	256 × 512	Y			Y	
EC-Earth3-CC	256 × 512	Y		Y		Y
EC-Earth3-Veg	256 × 512	Y	Y	Y	Y	Y
EC-Earth3-Veg-LR	160 × 320	Y	Y	Y	Y	Y
FGOALS-f3-L	180 × 288	Y				
FGOALS-g3	80 × 180	Y	Y	Y	Y	Y
GFDL-ESM4	180 × 288	Y	Y	Y	Y	Y
IITM-ESM	94 × 192	Y	Y	Y	Y	Y
INM-CM4-8	120 × 180	Y	Y	Y	Y	Y
INM-CM5-0	120 × 180	Y	Y	Y	Y	Y
IPSL-CM5A2-INCA	96 × 96	Y	Y		Y	
IPSL-CM6A-LR	143 × 144	Y	Y	Y	Y	Y
KACE-1-0-G	144 × 192	Y	Y	Y	Y	Y
KIOST-ESM	96 × 192	Y	Y	Y		Y
MIROC6	128 × 256	Y	Y	Y	Y	Y
MPI-ESM-1-2-HAM	96 × 192	Y				
MPI-ESM1-2-HR	192 × 384	Y	Y	Y	Y	Y
MPI-ESM1-2-LR	96 × 192	Y	Y	Y	Y	Y
MRI-ESM2-0	160 × 320	Y	Y	Y	Y	Y
NorESM2-LM	96 × 144	Y	Y	Y	Y	Y
NorESM2-MM	192 × 288	Y	Y	Y	Y	Y
SAM0-UNICON	192 × 288	Y				
TaiESM1	192 × 288	Y	Y	Y	Y	Y

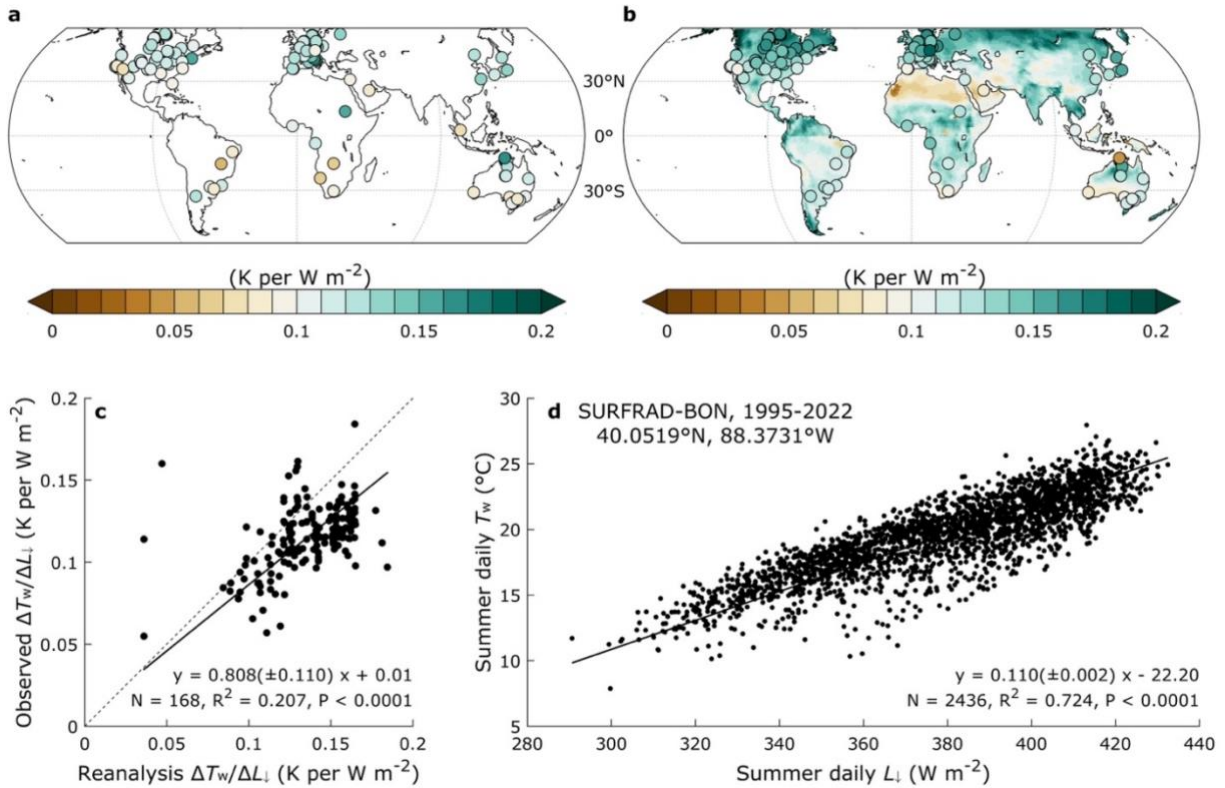


**Figure S1.** Observed sensitivity of the wet-bulb temperature to the surface downward longwave radiation. (a) Spatial distribution of the sensitivity at the 168 surface radiation measurement sites. (b) Spatial distribution of the sensitivity according to atmospheric reanalysis. (c) Spatial correlation between observed and reanalysis sensitivity. (d) Relationship between the wet-bulb temperature  $T_w$  and the surface downward longwave radiation  $L_{\downarrow}$  at Bondville (BON), Illinois, USA. Solid lines in (c)-(d) represent linear relationships with regression statistics noted. Dashed line in (c) is 1:1.

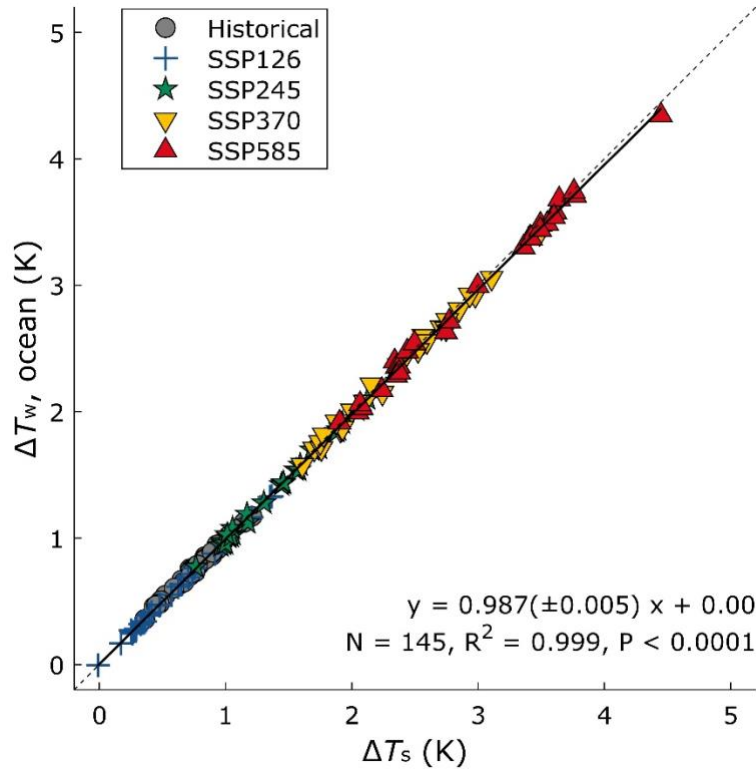


**Figure S2.** Identical changes of the ocean surface temperature and the oceanic wet-bulb temperature. Solid line represents linear relationship with regression statistics noted. Dashed line is 1:1.

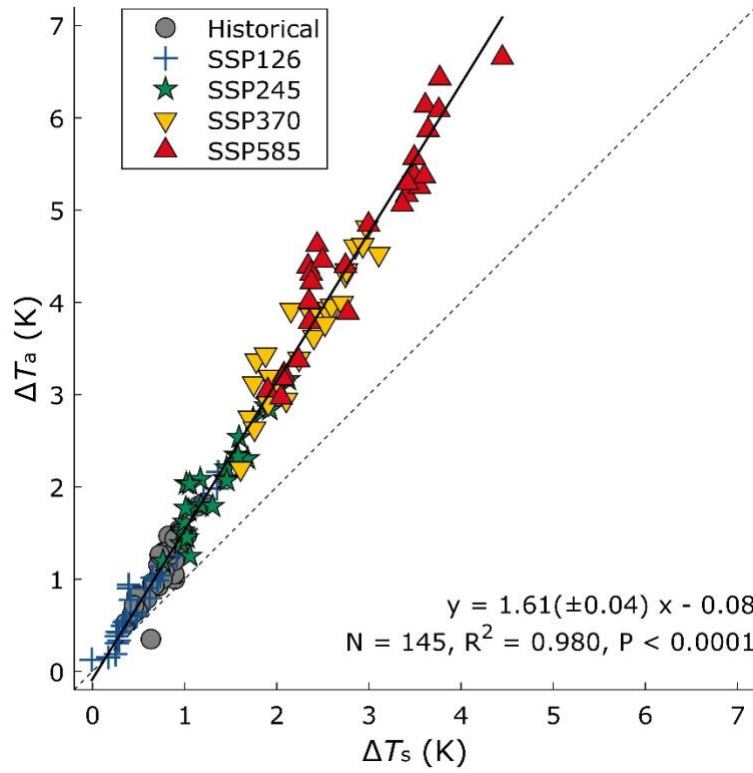


**Figure S3.** Amplification of the land air temperature change in reference to the ocean surface temperature. Solid line represents linear relationship with regression statistics noted. Dashed line is 1:1.

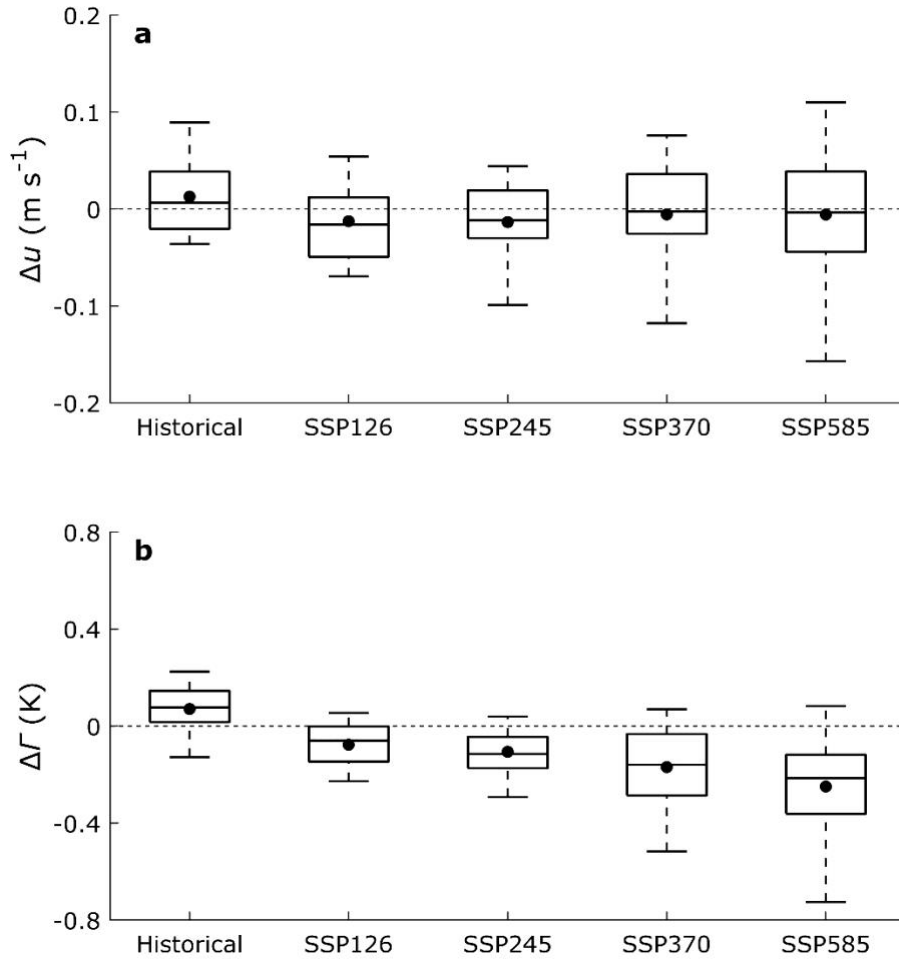


**Figure S4.** Changes in the land surface wind speed and the static stability of the lower troposphere. (a) Scenario mean change of the land surface wind speed  $\Delta u$ . (b) Scenario mean change of the static stability of the lower troposphere  $\Delta \Gamma$ . Box plots show the median (line), 25–75% range (box), 5–95% range (whiskers) and the mean value (dot).

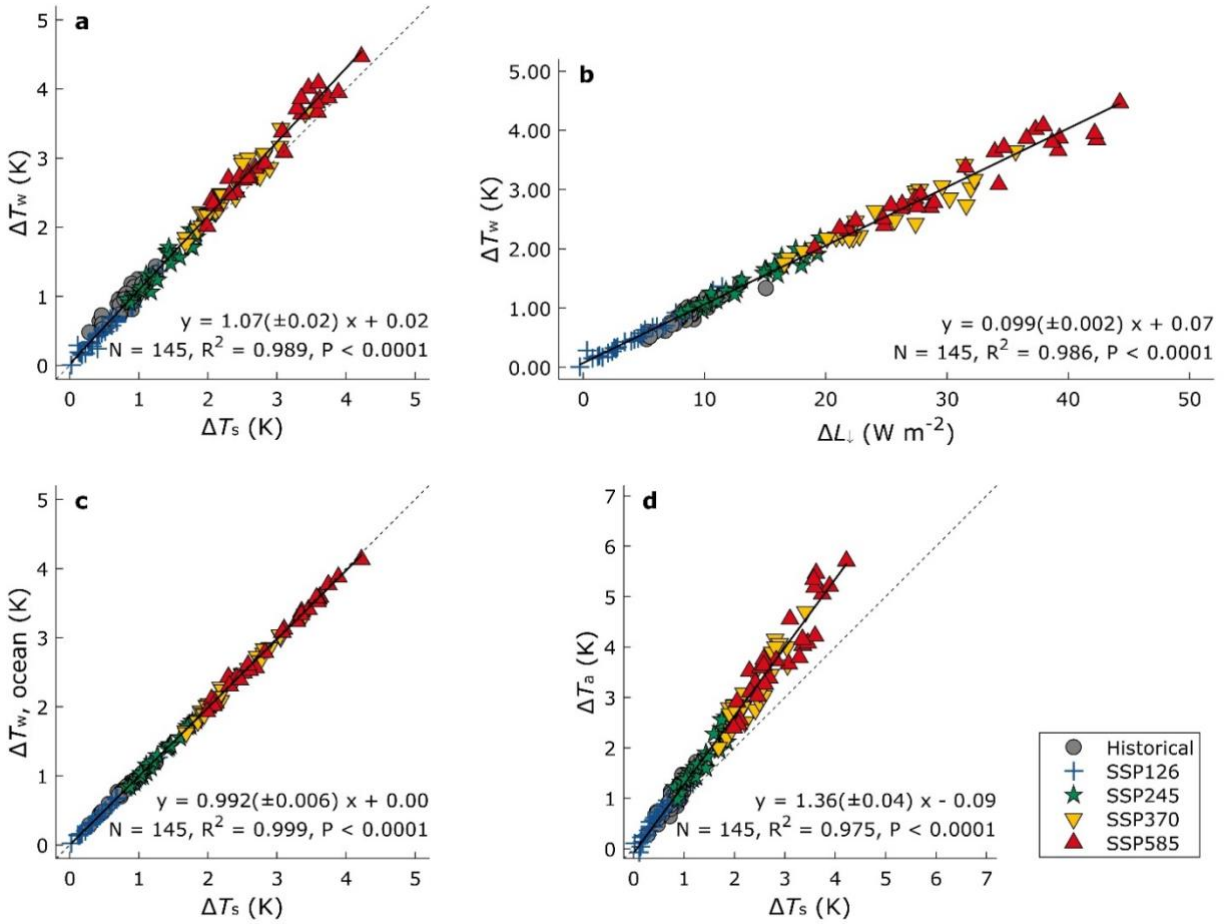


**Figure S5.** Climatology of land wet-bulb temperature for the tropical zone (20°S-20°N). (a) Relationship between changes in the land wet-bulb temperature and ocean surface temperature. (b) Relationship between changes in the land wet-bulb temperature and incoming longwave radiation at the surface. (c) Relationship between changes in the ocean surface wet-bulb temperature and ocean surface temperature. (d) Relationship between changes in the land air temperature and ocean surface temperature.

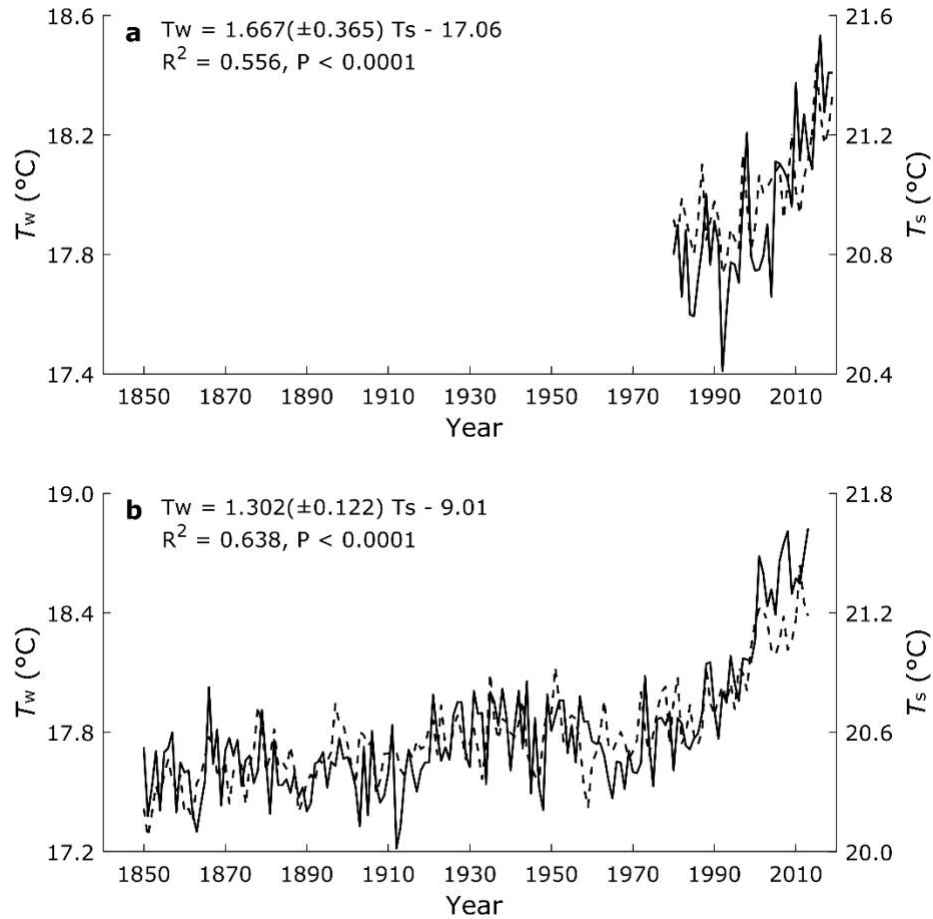


**Figure S6.** Oceanic control on the land wet-bulb temperature change at interannual time scale. (a) Interannual changes of the wet-bulb temperature  $T_w$  and the ocean surface temperature  $T_s$  according to NCEP-R1 reanalysis. (b) As in (a) except from CESM2-WACCM historical model simulation. Solid and dashed lines represent  $T_w$  and  $T_s$ , respectively. The statistics of linear regression are also shown.

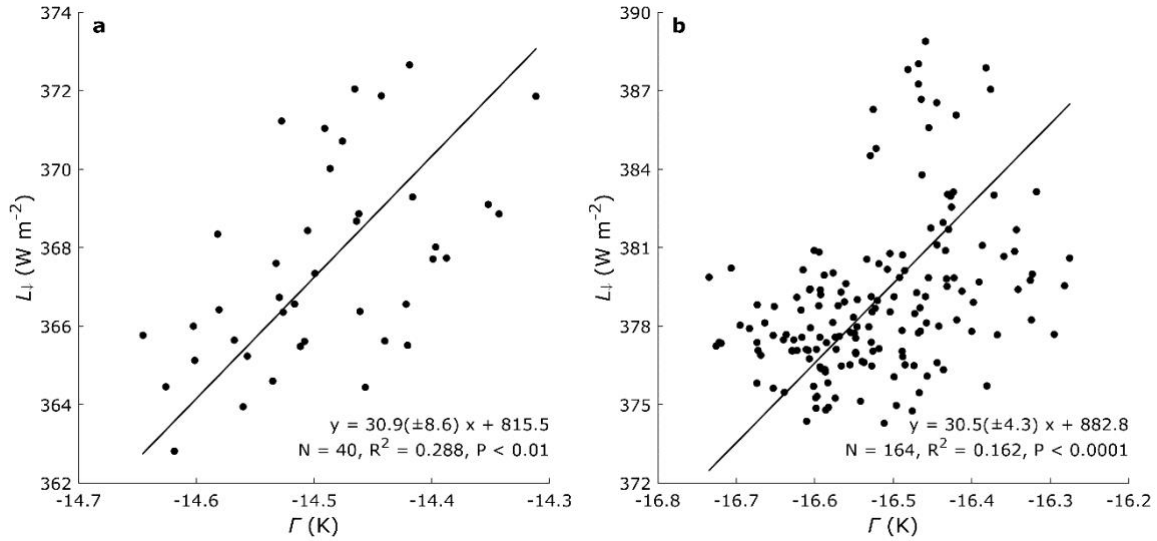


**Figure S7.** Stronger downward longwave radiation with increasing stability of the lower troposphere. (a) Relationship between the surface downward longwave radiation  $L_{\downarrow}$  and the tropospheric static stability  $\Gamma$  according to NCEP-R1 reanalysis. (b) As in (a) except from CESM2-WACCM historical model simulation. Solid lines represent linear relationships with regression statistics noted.